Arabian Journal of Chemistry (2020) **13**, 5939–5948

King Saud University

Arabian Journal of Chemistry

www.ksu.edu.sa
www.sciencedirect.com

ORIGINAL ARTICLE

Synergetic effect of $ZnIn_2S_4$ nanosheets with metal-organic framework molding heterostructure for efficient visible- light driven photocatalytic reduction of Cr(VI)

Muhammad Bilal Hussain *, **Umair Azhar, Herman Maloko Loussala, Rameez Razaq**

Key Laboratory of Interfacial Reaction & Sensing Analysis in University of Shandong, School of Chemistry and Chemical Engineering, University of Jinan, Jinan 250022, Shandong, PR China

Received 13 March 2020; accepted 23 April 2020
Available online 30 April 2020

KEYWORDS

Synergetic effect of $ZnIn_2S_4$ nanosheets;
Photocatalytic Cr(VI) reduction;
Visible light;
Solvothermal approaches;
Solar light harvestation;
Varying amount of UiO-66-NH_2

Abstract The photocatalytic reduction of toxic Cr(VI), to green Cr(III) by visible light, is highly required. Metal-organic frameworks have been waged more and more devotion in the field of environmental remediation. Diversification along with functionalization is still thought-provoking and crucial for the progress of metal-organic framework (MOF)-based high activity materials. Herein, a succession of UiO-66-NH_2@$ZnIn_2S_4$ composites with varying amount of UiO-66-NH_2 is prepared by the facile solvothermal technique. Synergetic effect for Cr(VI) reduction is assessed under the influence of visible light ($\lambda > 420$ nm). UiO-66-NH_2 octahedron is detained by $ZnIn_2S_4$ nanoflakes. The obvious enhancement in activity is observed which is credited to the well-suited energy band construction and close interaction between the interface of $ZnIn_2S_4$ and UiO-66-NH_2, which leads to effective transfer and separation of photogenerated carriers. Synergistic effect could be evidently understood from the PL and UV -spectroscopy, after molding into heterostructure of UiO-66-NH_2@$ZnIn_2S_4$. In addition, UiO-66-NH_2@$ZnIn_2S_4$ composites exhibited good stability in photocatalytic reduction. Consequently, this UiO-66-NH_2 constructed composite has high potential in the field of environmental remediation.

1. Introduction

A boost in expanding water pollution due to the expeditious growth of urbanization and industrialization resulted in a deliberate environmental issue throughout the globe (Bai et al., 2018; Hussain et al., 2020; Liu et al., 2020; Wang et al., 2019; Zhang et al., 2018). Hexavalent chromium (VI),

* Corresponding author.
E-mail address: bilal.fcc288794@qq.com (M.B. Hussain).

Peer review under responsibility of King Saud University.

Production and hosting by Elsevier

https://doi.org/10.1016/j.arabjc.2020.04.029
1878-5352

which is highly soluble, toxic and carcinogenic in heavy metal pollutants, poses a serious threat to ecosystem (Liu et al., 2020; Zhang et al., 2014). Therefore, in the early phase, lots of approaches along with skills have been entrenched to eliminate wastewater Cr(VI), including ion-exchange method (Xing et al., 2007), membrane separation (Divrikli et al., 2007), chemical precipitation and adsorption (Xie et al., 2017). Nevertheless, the conventional means have the disadvantages of high cost, high energy utilization, poor performance and low removal rate, which hinder their comprehensive applications (Zhao et al., 2017). As an effective, green and efficient method, the photocatalytic reduction has been emerged as an effective strategy in the remediation of Cr(VI) pollutants as compared to traditional methods (Padhi et al., 2017).

The benefits of reduction by photocatalysis contain high efficacy, little cost, no production of pollution at the secondary level and direct utilization of the energy from the solar origin (Guo et al., 2019a; Guo et al., 2019b; Zhang et al., 2011b). Contrary to, single component photocatalyst, composite photocatalyst have the capability to heighten the efficacy of photocatalysis, chiefly due to the heterojunctions which contribute to the separation of electrons as well as the holes through the interface transfer of charge (Liu et al., 2015; Zhang et al., 2011a; Zhang et al., 2014). For instance, Tian and his colleagues prepared Mn_3O_4@ZnO/Mn_3O_4 heterojunction and reduced Cr(VI) by photocatalysis. The new photocatalyst has good Cr(VI) activity (200 mL, 10 mg/L) and demonstrated complete reduction after 70 min (Zhao et al., 2017). The magnetic and rectifiable TiO_2/Fe_3O_4 heterostructures have been successfully synthesized by sounak' group. In the aerobic atmosphere, the photocatalytic ability of Cr(VI) photoreduction is stronger than that of bulk TiO_2. Undoubtedly TiO_2/Fe_3O_4 junction has the ability to promote the charge generation and hide the charge recombination mechanisms (Challagulla et al., 2016). That is why a jillion studied the utilization of a series of composite photocatalysts to reduce Cr (VI) by photocatalysis (Shen et al., 2013a).

Metal-organic frameworks (MOFs) are kind of materials having pores with the crystal structure of three-dimensions made up of metal units and organic ligands. As a consequence of its broadening particular surface area, exclusive structure having adjustable pore size, MOFs have a wide application prospect in the fields of gas adsorption, separation, chemical sensing, drug delivery and catalysis (Xiao et al., 2016). The current advancement in research shows that some MOFs have excellent properties as semiconductors and can be utilized for photocatalysis (Zhao et al., 2017). A large number of MOFs-based photocatalysts have applications in the elimination of organic pollutants (Shi et al., 2015), hydrogen production (Wu et al., 2017; Yang et al., 2016), CO_2 reduction (Fu et al., 2012) organic transformations (Li et al., 2014) and especially in the reduction of Cr(VI) (Shen et al., 2013b) which is more described at present. As compared to the traditional semiconductor photocatalyst, MOF-based photocatalyst has greater application value, owing to the significant adjustments of metal-oxygen clusters and bridging organic connectors that can tolerate appropriate tuning and reasonable molecular design of photocatalyst, which is very reasonable (Yang et al., 2016).

In addition, the specific porosity of MOFs makes the substrate then products diffuse by accessible framework structure (Furukawa et al., 2014). Although MOF is believed to be a quickly developing attraction, the MOFs-based derivatives used for photocatalytic activity are still in the initial phase of research (Vermoortele et al., 2013). After photoexcitation, MOFs can perform electron-hole recombination at a very high rate like all single component photocatalysts (Zhao et al., 2017). The metal, ligand substitution and deposition of noble metals can be utilized to enhance the efficacy of photocatalysis of MOFs (He et al., 2016). In addition, the combination of MOFs and collector semiconductor materials to develop heterostructure is also a possible way of boosting the photocarriers separation and improving the efficiency of photocatalysis (Chambers et al., 2017). Lately, the synthesis of semiconductor @ MOF heterostructures like TiO_2@UiO-66-NH_2 (Dennis T. Lee et al., 2017), $ZnIn_2S_4$@MIL-125(Ti) (Liu et al., 2018), MoS_2 @ UiO-66@CdS (Shen et al., 2015), UiO-66-NH_2@C_3N_4 (Shen et al., 2014), ZnO@ZIF-8 (Wang et al., 2016), $BiVO_4$@MIL-101 (Xu et al., 2015), BiOBr@UiO-66 (Tong et al., 2018), CdS@UiO-66-NH_2 (Shen et al., 2013a) and $Cd_{0.2}Zn_{0.8}S$ @UiO-66-NH_2 (Su et al., 2017) expressed countless benefits because of synergistic effect. $ZnIn_2S_4$, a chalcogenide compound, has a suitable band gap, ranging from 2.34 eV to 2.48 eV, which is in good agreement with visible light absorption. However, to the best of our knowledge, no work related to UiO-66-NH_2@ $ZnIn_2S_4$ has been done before.

Herein, we firstly reported the successful integration of $ZnIn_2S_4$ with UiO-66-NH_2 *via* a new facile solvothermal method along with good morphology as a visible-light photocatalyst for reduction of Cr(VI) with efficient performance. The UiO-66-NH_2@ $ZnIn_2S_4$ composite with different concentrations of UiO-66-NH_2 has been effectively optimized. The synergistic effect could be clearly understood from the PL and UV -spectroscopy, after molding into heterostructure of UiO-66-NH_2@$ZnIn_2S_4$, optimum amount of UiO-66-NH_2 have obtained with enhanced band gap resulted in more visible light absorption and reduced recombination of electron and hole. The UiO-66-NH_2@$ZnIn_2S_4$ has shown excellent photocatalytic performance for the reduction of Cr(VI) under the irradiation of visible light. The outstanding performance towards the photocatalytic reduction of Cr(VI) is due to the synergistic effect of $ZnIn_2S_4$ and UiO-66-NH_2 which cause the efficient electron-hole separation and suppression in recombination. 20UN@ZIS shows excellent efficiency among these composites because of the high solubility and adsorption capacity of Cr(VI) metal ions in water. Moreover, the UiO-66-NH_2@$ZnIn_2S_4$ composite exhibited excellent stability and recyclability which plays a vital role in wastewater treatment. It is hoped that these types of photocatalyst can expose a novel space for new stratagem of MOFs based nano-composites in the future.

2. Experimental

2.1. Materials

N, N-dimethylformamide (DMF, 99.9%), sodium sulfate (Na_2SO_4, 99.9%) were purchased from Sinopharm Chemical Reagents Co. Ltd. Zirconium (IV) chloride ($ZrCl_4$, 99.9% metals basis), and diphenyl carbazide (DPC, 98%) were bought from Shanghai Macklin Biochemical Co. Ltd. Ethanol and Ethylene glycol (, 99.9%) were attained from Xilong

Incorporated Chemical Industry Co. Ltd., 2-Aminoterephthalic acid [$H_2NC_6H_3$-1,4-$(CO_2H)_2$, 98%] was bought from Beijing HWRK Chem Co., Ltd., Milli-Q H_2O purification system provided the pure H_2O water for its use in experiments. No further purification was required for the use of these analytical grade chemicals.

2.2. Preparation of UiO-66-NH_2

Particularly, 5 mL DMF solution of $ZrCl_4$ (9 mM) and 5 mL DMF solution of NH_2-BDC (8 mM) were taken in glass bottle separately and mixed in third glass vial along with the addition of 1.2 mL of acetic acid. The sample was heated at 120 °C overnight without any stirring. Finally, the obtained product was first centrifuged and then washed several times first with DMF then with water and lastly with ethanol. The UiO-66-NH_2 attained was activated at 50 °C overnight in an oven just to remove the solvent. UiO-66 was synthesized according to the same procedure as described above.

2.3. Preparation of UiO-66-NH_2@$ZnIn_2S_4$

The UiO-66-NH_2@$ZnIn_2S_4$ composites were synthesized by the facile solvothermal method. As a description, the specific concentration of UiO-66-NH_2 octahedral was ultrasonically dissolved into 15 mL of DMF and 5 mL EG cooperatively. Later $ZnCl_2$ (0.102 g), $InCl_3{\cdot}4H_2O$ (0.331 g) and thioacetamide (TAA) (0.150 g) were further mixed and stirred for 2 h. The resulting final solution was heated at 120 °C in oil for 12 h. After cooling the solid product washed mechanically with H_2O and ethanol, respectively. Then it was dried at 75 °C overnight. For comparison, the pure $ZnIn_2S_4$ was also synthesized by the same solvothermal process without the addition of UiO-66-NH_2. Similarly, UiO-66-NH_2 was also synthesized by following the method mentioned in the literature (Xiao et al., 2016).

2.4. Characterization

TEM (JEM-1400) was used to characterize the products. For the measurement of XRD, D8 Focus X-ray with Cu Kα radiation (λ = 0.15418 nm) was used and the sample was put on a silicon substrate. UV–Vis-NIR spectrophotometer (Shimadzu UV-3101PC) was used to measure the DRS. PL lifetime and PL photoluminescence were measured on Transient State Fluorescence and Edinburgh FLS920 Multifunction Steady State.

2.5. Photoelectrochemical measurements

Solartron analytical electrochemical analyzer (ModuLab XM) was used for photoelectrochemical measurements, which is a three-electrode system, in which Ag/AgCl (KCl, 3 M) acted as reference electrode and Pt foil as a counter electrode. 10 mg sample dipped in ethanol was put on the surface of dry ITO glass substrate which acted as working electrodes. To dry the sample for EIS and TPR, substrate was put into air for ten minutes and later heated at 80 ^{0}C for just five minutes. Consequently, all the electrodes were dipped into a quartz cell having 0.3 M Na_2SO_4 aqueous solution. Bias potential of 0.6 V was applied to measure the TPR for 60 s on/off chopped lighting. Alternating current voltage was applied to measure the EIS with an amplitude of 10 mV and the range of frequency was from 4 MHz to 100 MHz.

2.6. Photocatalytic activity measurements

300 W Xe arc lamp with a 420 nm cutoff filter was used to investigate the activity of the following samples UiO-66-NH_2, UiO-66-NH_2@$ZnIn_2S_4$ and $ZnIn_2S_4$ for the Cr(VI) reduction. To obtain absorption-desorption equilibrium before illumination, the suspension was stirred magnetically for 30 min in the dark at room temperature. For Cr(VI) reduction, the source chosen was Potassium dichromate. The reduction was done in an apparatus containing 20 mg catalyst at 30 °C and 40 mL of 50 mg/L Cr(VI) solution. Diphenyl carbazide (DPC) method was used to investigate the Cr (VI) contents in the solution. 200 μL of the reaction solution was dissolved with 1.8 mL of 0.2 M H_2SO_4 in a 2 mL tube. Then, 0.40 μL from newly prepared 0.25% (w/v) DPC in acetone was supplementary added into the above solution. To make sure the color development, the solution was shacked for thirty seconds and purple color formed having absorption at 540 nm was observed. By dividing C over C_0 the photocatalytic efficiency was determined where C means left concentration of Cr(VI) and C_0 the starting concentration of Cr(VI). While making use of performance of composite, the stability and reusability of the composite were determined. At least four-time same performance was observed from the composite. The photocatalyst was separated after each cycle and was washed, dried and reused.

3. Results and discussion

3.1. X-ray characterization

X-ray diffraction was used to determine the phase structure of samples. As shown in (Fig. 1), there were diffraction peaks at 2 θ = 21.1°, 27.7°, 47.5°, 52.4° and 56.4°. These peaks were related to (0 0 6), (1 0 2), (1 1 0), (1 1 6) and (0 2 2) crystal planes of hexagonal $ZnIn_2S_4$ (JCPDS No.65-2023) (Liu et al., 2018). UiO-66-NH_2 showed the same diffraction peaks as reported in the literature (Kandiah et al., 2010). For the

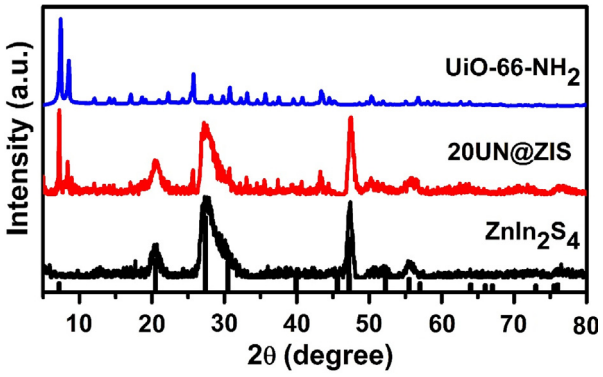

Fig. 1 The powder X-ray diffraction (PXRD) pattern of UiO-66-NH_2, UiO-66-NH_2@ $ZnIn_2S_4$- core-shell NPs and $ZnIn_2S_4$.

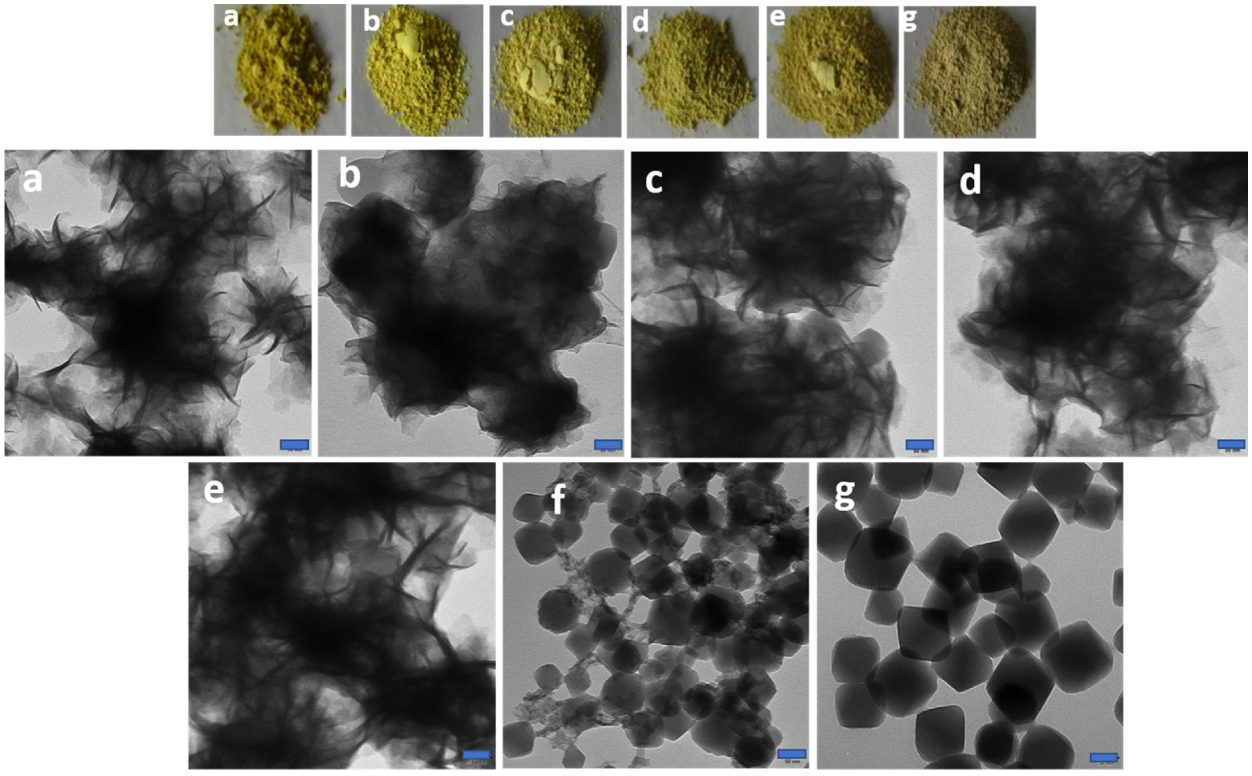

Fig. 2 TEM images of (a) $ZnIn_2S_4$, (b) 10UiO-66-NH_2@$ZnIn_2S_4$-NPs (c) 20UiO-66-NH_2@$ZnIn_2S_4$-NPs (d) 30UiO-66-NH_2@$ZnIn_2S_4$-NPs (e) 40UiO-66-NH_2@$ZnIn_2S_4$-NPs (f) 50UiO-66-NH_2@$ZnIn_2S_4$-NPs and (g) UiO-66-NH_2 -NPs. Scale bar for each image is 50 nm.

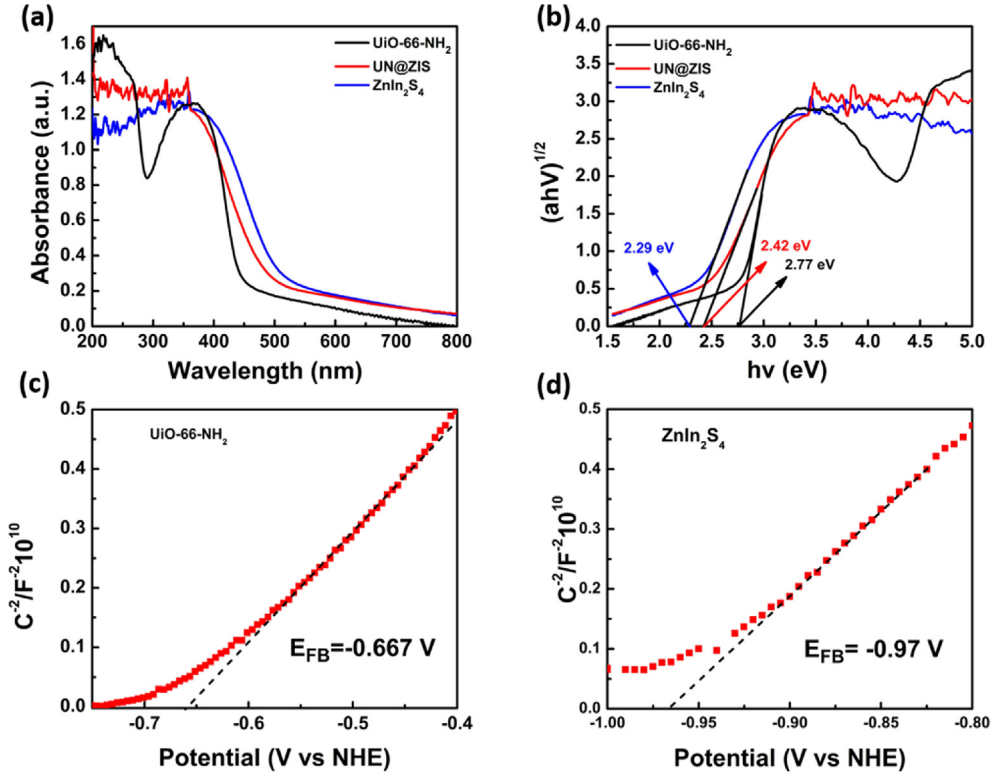

Fig. 3 (a) UV–Vis diffuse reflectance spectra (DRS), and (b) band-gap values assessed by a correlated curve of $(ahv)^{1/2}$ set against photon energy plots of the as-synthesized UiO-66-NH_2@$ZnIn_2S_4$-NPs core-shell NPs. Mott-Schottky plot for (c) UiO-66-NH_2 and (d) $ZnIn_2S_4$ nanosheets electrode in saturated Na_2SO_4 electrolyte solution (0.1 M, pH = 6.8) vs NHE.

UiO-66-NH_2@$ZnIn_2S_4$ sample, all peaks of the original material coexisted uniformly in the 20UN@ZIS composite.

3.2. Morphological characterization

UiO-66-NH_2 demonstrated octahedral morphology with sharp edge and flat surface (Fig. 2g). The average diameter of octahedron was about 150 nm, which provided a good environment for the assembly of Photocatalysts. The original $ZnIn_2S_4$ had the morphology of microspheres, each of which was composed of many nanoflakes, cross-linked to each other. Low and high magnification TEM images of pure $ZnIn_2S_4$ are shown in (Fig. 2a). $ZnIn_2S_4$ microspheres grew uniformly and compactly on the surface of UiO-66-NH_2. After hybridizing with UiO-66-NH_2, $ZnIn_2S_4$ microspheres were consistently dispersed on external of UiO-66-NH_2 octahedron, and UiO-66-NH_2 was completely encapsulated by $ZnIn_2S_4$ sheets. Composite structures of the two layers were evidently observed. Visually, $ZnIn_2S_4$ nanosheets formed the outer layer connected to the surface of UiO-66-NH_2 giving sphere-like morphology keeping the UiO-66-NH_2 in inner layer. In addition, $ZnIn_2S_4$ nanosheets were connected with each other and conducive to transferring the electrons between both materials. A series of different contents of UiO-66-NH_2, in the UiO-66-NH_2@$ZnIn_2S_4$, were prepared (Fig. 2). By changing the concentration of UiO-66-NH_2 from 10% to 50%, in weight, the morphology of the composite changed slightly. When it reached 50%, the formation process was stopped, as shown in (Fig. 2f). And it can be proved by studying their performance (Fig. S1).

3.3. Optical characterization

UV–Vis diffuse reflectance spectroscopy was used to measure the absorption characteristics of pristine UiO-66-NH_2, $ZnIn_2S_4$ and the composite with the specific concentration of UiO-66-NH_2 Fig. 3(a). Pure UiO-66-NH_2 had an absorption edge in the visible region (Shen et al., 2013b). Pure $ZnIn_2S_4$ had an absorption edge at 600 nm, related to intrinsic band gap absorption (Liu et al., 2018). Comparatively UiO-66-NH_2@$ZnIn_2S_4$ composite showed a longer absorption edge than the pure UiO-66-NH_2. Red-shift specified more absorption of visible light along with more production of electron and hole pairs by the composite. The band gap energy (Eg) of the sample can be obtained from the graph of the relationship between $(\alpha hV)^{1/2}$ and photon energy (hv). The (Eg) values UiO-66-NH_2, 20UN@ZIS and $ZnIn_2S_4$ were estimated to be 2.75, 2.42 and 2.29 EV, respectively (Fig. 3b) (Shen et al., 2013b; Zhang et al., 2018). In addition, according to the principle of light reflection spectrum, the light reflectivity on the surface of high-density composite 20UN@ZIS is generally lower than the original $ZnIn_2S_4$. Specifically, the surface of

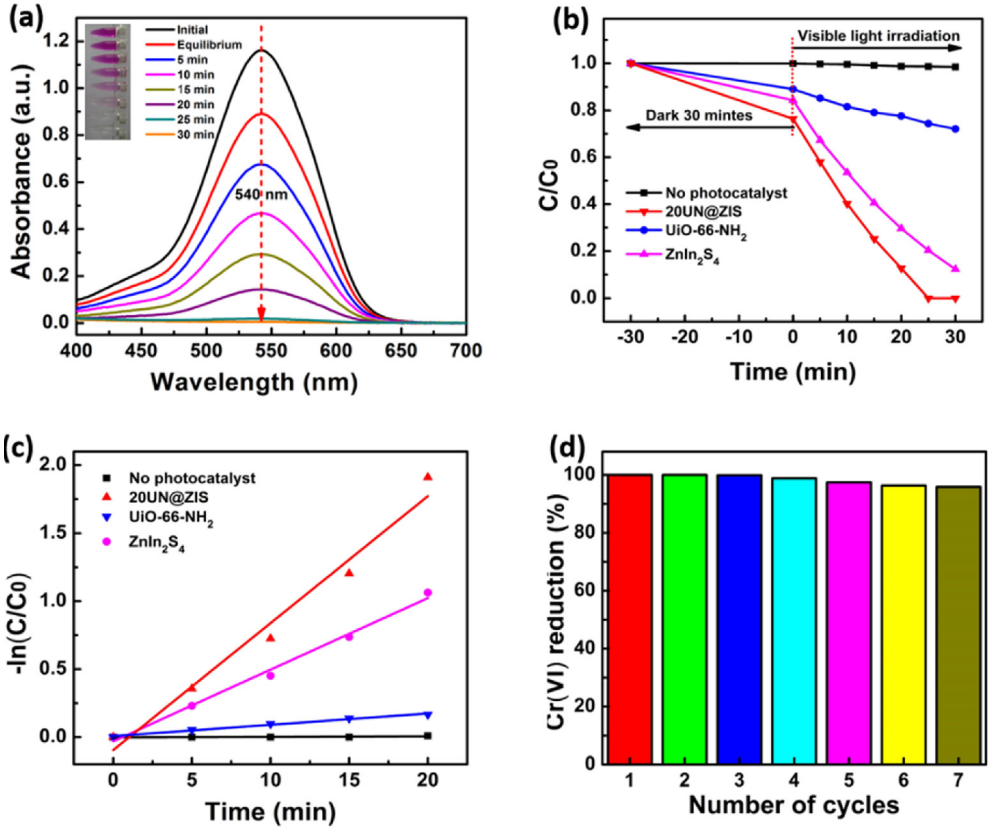

Fig. 4 (a) UV–Vis spectra along with color (inset) change of Cr(VI) aqueous solution in the existence of UiO-66-NH_2@$ZnIn_2S_4$ core-shell NPs under the visible irradiation with a 300 W Xenon lamp at room temperature. (b) The reduction consequences (C/C_0) of several photocatalysts on Cr(VI) under the similar condition, (c) The matching kinetic plots for the reduction of Cr(VI). (d) The various reduction results of Cr(VI) with UiO-66-NH_2@ $ZnIn_2S_4$ core-shell NPs.

Table 1 Data comparison of photocatalytic Cr(VI) reduction over different catalysts.

Sample	Sample (mg)	$K_2Cr_2O_7$ (mg/L)	volume (mL)	Time (min)	References
20UN@ZIS	20 mg	50 mg/L	40 mL	30	This study
$ZnIn_2S_4$/CdS	50 mg	50 mg/L	50 mL	30	(Zhang et al., 2018)
TiO_2/$ZnIn_2S_4$	40 mg	50 mg/L	40 mL	60	(Li et al., 2020)
CNFs/$ZnIn_2S_4$	40 mg	50 mg/L	40 mL	60	(Qiu et al., 2019)
Bi_2S_3/BiOCl@$ZnIn_2S_4$	40 mg	50 mg/L	40 mL	60	(Qiu et al., 2020)
$CaIn_2S_4$/$ZnIn_2S_4$ un	50 mg	20 mg/L	50 mL	30	(Xu et al., 2018)

.

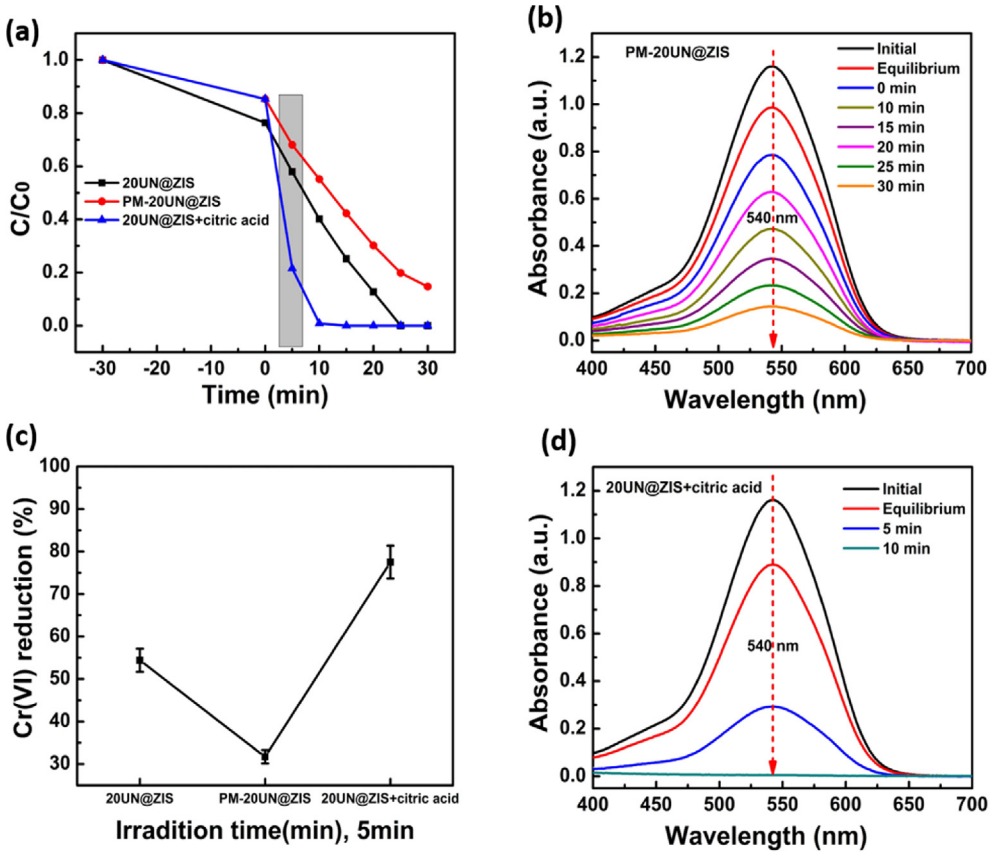

Fig. 5 (a), (c) Assessment of the Photocatalytic Cr(VI) reduction efficacies over 20UN@ZIS, PM-20UN@ZIS and 20UN@ZIS + 0.5 mL citric acid. (b), (d) UV–vis absorption spectra of Cr(VI) solution treated with PM-20UN@ZIS and 20UN@ZIS + 0.5 mL citric acid.

the composite can improve the light absorption efficiency of 20UN@ZIS, which is verified by the light absorption calculation of UV–Vis diffuse reflectance spectrum Fig. 3(b). 20UN@ZIS demonstrated enhanced light absorption in the visible light region. It is confirmed that 20UN@ZIS has a higher light absorption capacity than the original $ZnIn_2S_4$, which is of great significance to improve photocatalytic efficiency.

The band gap of 20UN@ZIS calculated by square root absorption method was 2.42 eV, which was higher than the original $ZnIn_2S_4$ (2.29 eV), fell in between two semiconductors. It indicated the formation of heterostructure magnificently. Meanwhile, the recombination of electrons and holes was suppressed due to the core-shell heterostructure. In sense, its performance was significantly enhanced as compared to pristine UiO-66-NH_2 and $ZnIn_2S_4$.

The flat band potential of UiO-66-NH_2 was also derived from the mott-schotky plots which was about −0.82 V vs. Ag/AgCl (i.e. −0.72 V vs. NHE). The bottom of many semiconductors is n-type if it is more negative by 0.1 V as compared to the flat band potential. The CB of UiO-66-NH_2 was estimated to be −0.667 V vs. NHE. Similarly, the (E_{VB}) value of UiO-66-NH_2 was calculated to be +2.02 V vs. NHE as shown in Fig. 3(c).

The calculated E_{VB} and E_{CB} values of $ZnIn_2S_4$ are +1.32 eV and −0.97 eV, respectively.

A typical n-type mott-Schottky plot of $ZnIn_2S_4$ and UiO-66-NH_2 was measured at frequency range of 1000 to 2000 Hz as presented in Fig. 3(d).

3.4. Photocatalytic activity

The photocatalytic activity of Cr(VI) in aqueous solution was investigated under the influence of visible light. Fig. 4(a) shows the reduction efficacy of Cr(VI) of UiO-66-NH_2@$ZnIn_2S_4$. It was observed that Cr(VI) absorption decreased steadily at 540 nm and disappeared completely after 30 min. Every time, the color of the reaction solution changed from pink to colorless (inset Fig. 4(a)), indicated that Cr(VI) was reduced to Cr (III) during photocatalytic reduction. The UiO-66-NH_2 as a photocatalyst, exhibited lower performance of Cr (VI) reduction compared with $ZnIn_2S_4$ (Fig. 4b).

The photocatalytic activity of $ZnIn_2S_4$ with Cr(VI) concentration of 50 mg/L, UiO-66-NH_2 and $ZnIn_2S_4$ were in accordance with the literature (Shen et al., 2014; Zhang et al., 2018). After coupling with UiO-66-NH_2, the photocatalytic activity of $ZnIn_2S_4$ was significantly improved. The reduction of Cr(VI) in UiO-66-NH_2@$ZnIn_2S_4$ composite increased with the heightening the content of UiO-66-NH_2 and reached the maximum value when UiO-66-NH_2 content was left 20 wt%. However, a further increase in the content of UiO-66-NH_2 resulted in a decrease in Cr(VI) (Fig. S1). This may be due to the following factors: I- with the increase of UiO-66-NH_2, the related contents of $ZnIn_2S_4$ decreased, which is the most favorable active substance in the reaction. II- excess UiO-66-NH_2 may be converted into the composite midpoint of the charge, which can be confirmed by the photoluminescence results (Fig. 7(a)), which might be the reason for the decrease of Cr (VI) reduction. Therefore, choosing the appropriate amount of UiO-66-NH_2 is the key to obtain the best Cr(VI) reduction rate by using UiO-66-NH_2@$ZnIn_2S_4$ hybrid material. The results indicated that the order of the regularization rate is basically the same as that of the invention, and the 20UN@ZIS sample still showed the best efficiency (Table 1). In particular, the photocatalytic reduction rate of Cr(VI) by 20UN@ ZIS was higher than that by $ZnIn_2S_4$ based photocatalysts previously reported. For example, UiO-66-NH_2 (Shen et al., 2014),MIL-88(B)–NH_2(Fe)(Shi et al., 2015), UiO-66-NH_2@grephene (Shen et al., 2014), ZnO@ZIF-8 (Wang et al., 2016), Pd@UiO-66-NH_2(Shen et al., 2013c), CdS@ $ZnIn_2S_4$ (Zhang et al., 2018) and so on. Fig. 4(c) shows the relationship between ln (C/C_0) and irradiation time when Cr (VI) is reduced by several catalysts. The results show that the reaction rate was close to the first-order kinetics, that is, ln (C/C_0) = KT, where k is the first-order kinetics constant. The K value determined in advance by the corresponding linear curve slope pointed that the reaction rate constant of Cr(VI) reduction was 0.93 min^{-1} on the core–shell NPs of UiO-66-NH_2@ $ZnIn_2S_4$, which was 1.78 and 11.20 higher than that of $ZnIn_2S_4$ (0.052 min^{-1}) and UiO-66-NH_2 (0.0083 min^{-1}), respectively. Furthermore, 20UN@ZIS still maintained its high activity after several cycles of reduction reactions, which is very important in practical applications (Fig. 4d).

The physical mixture of UiO-66-NH_2 and $ZnIn_2S_4$ was passed through catalytic reduction just to confirm the effect of the composite. As shown in Fig. 5(a) the lower performance was observed by the mixture represented by PM-20UN@ZIS, compared with original composite 20UN@ZIS. Improvement in photocatalytic activity suggested that heterostructure was responsible for indorsing the electron transfer and parting. The effect of scavenger can be seen in Fig. 5(a). The rapid increase in the reduction of Cr(VI) was observed when citric acid was added. Under five minutes light illumination, the reduction of PM-20UN@ZIS and 20UN@ZIS + 0.5 mL citric acid were 31.7% and 75.5% respectively Fig. 5(c). The simplest approach to mechanism is that the adsorbed citric acid on the surface of the catalyst experienced oxidation by holes, meanwhile suppressing the recombination. The changes in the spectra of UV–vis absorption for the relevant materials are illustrated in Fig. 5(b) and (d).

TEM notes showed that after many reduction tests, the morphology of the core-shell NPs of UiO-66-NH_2@$ZnIn_2S_4$ was almost unaffected. In particular, the high density in the sphere can be clearly observed on the surface of the recovered UiO-66-NH_2@$ZnIn_2S_4$ core-shell NPs which reflects their outstanding stability in the photocatalytic reaction. In addition, according to the XRD and TEM results shown in Fig. 6(a), it was found that 20UN@ZIS can still maintain its original integrity after several photocatalytic cycles.

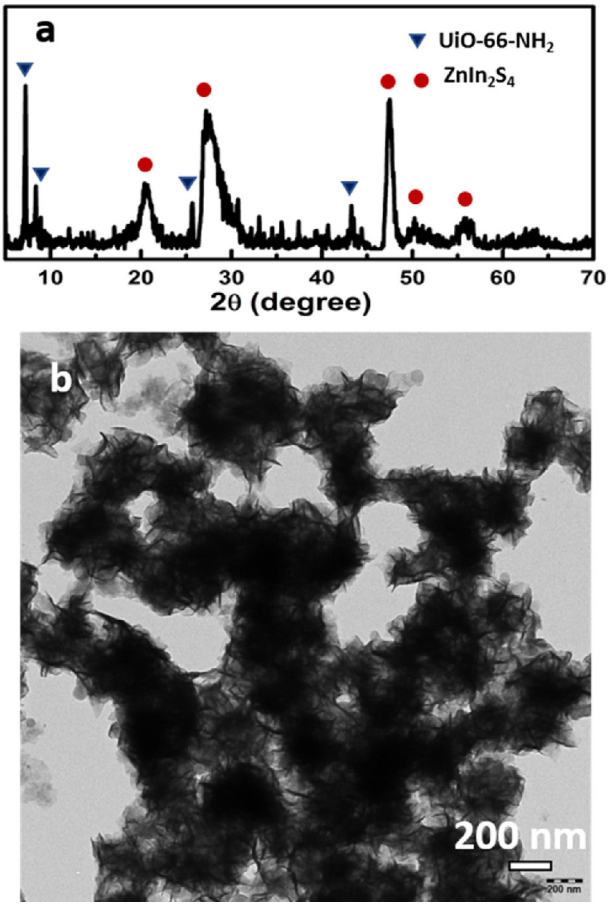

Fig. 6 (a) The powder X-ray diffraction (PXRD) pattern (b) TEM images of UiO-66-NH_2@$ZnIn_2S_4$-NPs core-shell NPs.

3.5. Photoluminescent characterization

PL can provide valuable information about the recombination and capture of charge carriers in semiconductors. Fig. 7(a) shows a comparison of the (PL) of various samples observed at an excitation wavelength of 310 nm. It can be seen that pure $ZnIn_2S_4$ had the highest emission peak near 445 nm. For 20NM@ZIS composite, the fluorescence peak was similar to the original $ZnIn_2S_4$, but an obvious decline in the intensity of the fluorescence peak was observed (Liu et al., 2015; Long et al., 2012). The obvious decline in the intensity of this fluorescence curve indicated a decline in the recombination rate of photogenerated e^- and h^+ in 20NM@ZIS system. In addition, the order of photoluminescence intensity was $ZnIn_2S_4$ > 40-NM@ZIS > 30NM@ZIS > 10NM@ZIS > 20NM@ZIS, which is in good agreement with the actual results of photocatalytic activity.

3.6. Transient photocurrent characterization

The photoelectrochemical properties can further test the charge separation ability. Fig. 7(b) shows a transient photocurrent response of UiO-66-NH_2, $ZnIn_2S_4$, and NH@ ZIS 40 under visible light. The original sample of UiO-66-NH_2 presented a small photocurrent density, which can be attributed to the rapid recombination of photogenerated electron and hole in UiO-66-NH_2. The observed transient photocurrent response of $ZnIn_2S_4$ was according to the literature. As compared to $ZnIn_2S_4$ and UiO-66-NH_2, 20UN@ZIS composite exhibited higher photocurrent intensity. These results confirmed that under the influence of light, the composite had a stronger ability to produce and transmit light-excited carriers(Shen et al., 2013c; Zhang et al., 2018).

3.7. Electrochemical impedance

In order to further validate the above-mentioned results and to study the development of interfacial charge motion, electrochemical impedance spectroscopy (EIS) was used. As compared to the diameters of $ZnIn_2S_4$ and UiO-66-NH_2 separately, it can be perceived that the Nyquist semicircle diameter of 20UN@ZIS composite was declined obviously, demonstrating the lower resistance of the composite and promoting the electron holes separation as well corresponding reduction Fig. 7 (c). On this basis, scheme 1 clarifies the photocatalytic activity mechanism of 20UN@ ZIS photocatalyst.

$ZnIn_2S_4$ has both conduction band (CB) and valance band (VB) higher than that of UiO-66-NH_2. When the composite was excited under visible light, both components generated electrons and holes, respectively as shown in Scheme 1 (Ge et al., 2019). In the interim, electron from the UiO-66-NH_2 CB transferred rapidly to the VB of $ZnIn_2S_4$ followed the route of direct Z-scheme. After coupling $ZnIn_2S_4$ with UiO-66-NH_2 photocatalyst, the photo-excited electrons in the CB of UiO-66-NH_2 recombined with the photogenerated holes in the VB of $ZnIn_2S_4$ photocatalyst, reserving the electrons in the CB

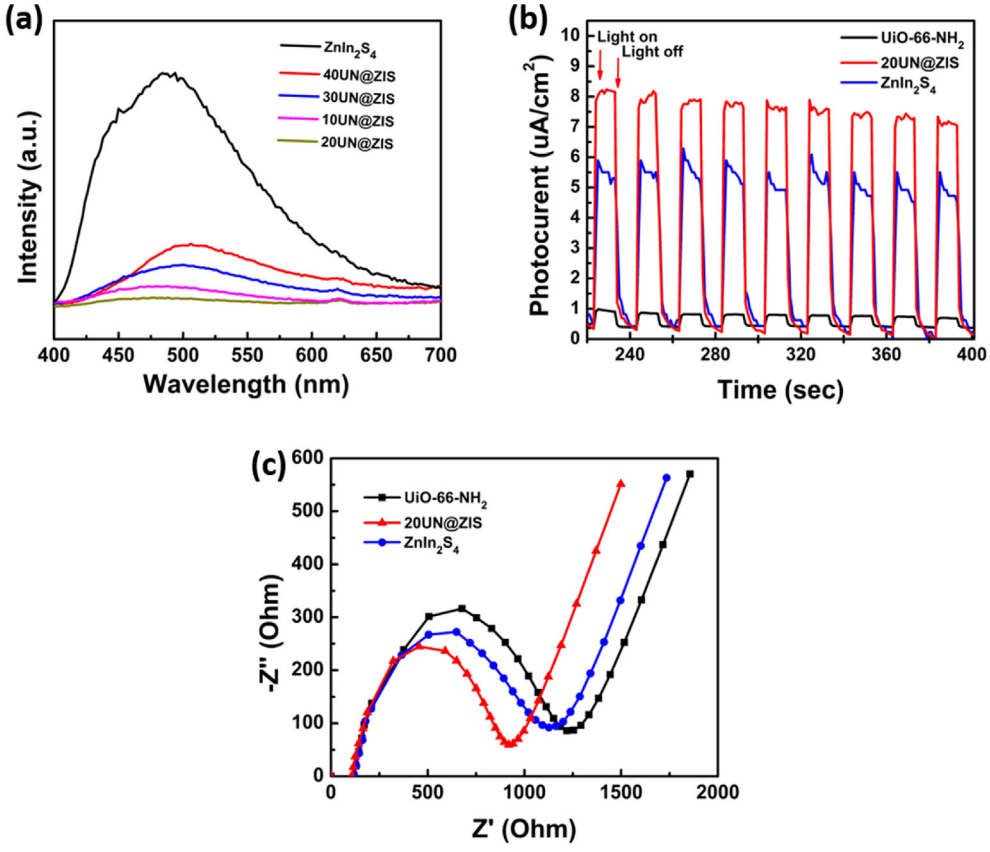

Fig. 7 (a) Photoluminescence spectra (PL), (b) transient photocurrent response, and (c) electrochemical impedance (EIS) spectra of UiO-66-NH_2@$ZnIn_2S_4$ core-shell NPs.

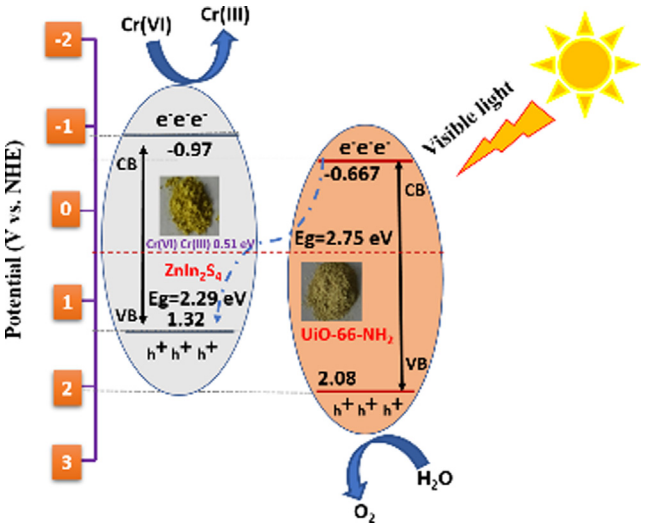

Scheme 1 Schematic illustration of Cr(VI) reduction mechanism over 20UN@ZIS core–shell NPs composite under the influence of visible light irradiation.

of $ZnIn_2S_4$ photocatalyst and holes in the VB of UiO-66-NH_2. This charge transfer route endows there served electrons and holes with high reduction and oxidation abilities (Liu et al., 2018; Long et al., 2012).

4. Conclusions

In conclusion, UiO-66-NH_2@$ZnIn_2S_4$ photocatalyst with high visible light driven activity was successfully synthesized by a facile solvothermal approach. A sequence of UiO-66-NH_2@$ZnIn_2S_4$ nano-composite with the variable content of UiO-66-NH_2 was prepared. Enhancement in the reduction activity of Cr(VI) was observed under the irradiation of visible light. The optimal content of UiO-66-NH_2 which exhibited high reduction activity and could participate distinctly in the reduction activity is 20%. The momentous improvement of photocatalytic performance of UiO-66-NH_2@$ZnIn_2S_4$ is credited to the subsequent two factors: (i) with the increase of UiO-66-NH_2, the related contents of $ZnIn_2S_4$ decreased, which is the most favorable active substance in the reaction; (ii) excess UiO-66-NH_2 may be converted into the composite midpoint of the charge, which was confirmed by the photoluminescence results. In addition, owing to having good reusability and stability, this work climaxes the intrinsic inspiration of MOFs on the recital of Cr(VI) reduction and also provides important guidance for making efficient photocatalyst with full utilization of the definite role of metal-organic frameworks.

Declaration of Competing Interest

The authors declare that they have no known competing financial interests or personal relationships that could have appeared to influence the work reported in this paper.

Appendix A. Supplementary material

Supplementary data to this article can be found online at https://doi.org/10.1016/j.arabjc.2020.04.029.

References

Bai, X., Du, Y., Hu, X., He, Y., He, C., Liu, E., Fan, J., 2018. Synergy removal of Cr (VI) and organic pollutants over RP-MoS_2/rGO photocatalyst. Appl. Catal. B: Environ. 239, 204–213.

Challagulla, S., Nagarjuna, R., Ganesan, R., Roy, S., 2016. Acrylate-based polymerizable sol-gel synthesis of magnetically recoverable TiO_2 supported Fe_3O_4 for Cr(VI) photoreduction in aerobic atmosphere. ACS Sustainable Chem. Eng. 4 (3), 974–982.

Chambers, M.B., Wang, X., Ellezam, L., Ersen, O., Fontecave, M., Sanchez, C., Rozes, L., Mellot-Draznieks, C., 2017. Maximizing the photocatalytic activity of metal-organic frameworks with aminated-functionalized linkers: substoichiometric effects in MIL-125-NH_2. J. Am. Chem. Soc. 139 (24), 8222–8228.

Divrikli, U., Kartal, A.A., Soylak, M., Elci, L., 2007. Preconcentration of Pb(II), Cr(III), Cu(II), Ni(II) and Cd(II) ions in environmental samples by membrane filtration prior to their flame atomic absorption spectrometric determinations. J. Hazard Mater. 145 (3), 459–464.

Fu, Y., Sun, D., Chen, Y., Huang, R., Ding, Z., Fu, X., Li, Z., 2012. An amine-functionalized titanium metal-organic framework photocatalyst with visible-light-induced activity for CO_2 reduction. Angew. Chem. Int. Ed. Engl. 51 (14), 3364–3367.

Furukawa, H., Gandara, F., Zhang, Y.B., Jiang, J., Queen, W.L., Hudson, M.R., Yaghi, O.M., 2014. Water adsorption in porous metal-organic frameworks and related materials. J. Am. Chem. Soc. 136 (11), 4369–4381.

Ge, H., Xu, F., Cheng, B., Yu, J., Ho, W., 2019. S-scheme heterojunction TiO_2/CdS nanocomposite nanofiber as H_2-production photocatalyst. ChemCatChem 11 (24), 6301–6309.

Guo, F., Li, M., Ren, H., Huang, X., Hou, W., Wang, C., Shi, W., Lu, C., 2019a. Fabrication of pn CuBi2O4/MoS2 heterojunction with nanosheets-on-microrods structure for enhanced photocatalytic activity towards tetracycline degradation. Appl. Surf. Sci. 491, 88–94.

Guo, F., Shi, W., Li, M., Shi, Y., Wen, H., 2019b. 2D/2D Z-scheme heterojunction of $CuInS_2$/g-C3N4 for enhanced visible-light-driven photocatalytic activity towards the degradation of tetracycline. Sep. Purif. Technol. 210, 608–615.

He, J., Yap, R.C.C., Yee Wong, S., Zhang, Y., Hu, Y., Chen, C., Zhang, X., Wang, J., Li, X., 2016. Controlled growth of a metal–organic framework on gold nanoparticles. CrystEngComm 18 (28), 5262–5266.

Hussain, M.B., Khan, M.S., Loussala, H.M., Bashir, M.S., 2020. The synthesis of a $BiOCl_x Br_{1-x}$ nanostructure photocatalyst with high surface area for the enhanced visible-light photocatalytic reduction of Cr (vi). RSC Adv. 10 (8), 4763–4771.

Kandiah, M., Nilsen, M.H., Usseglio, S., Jakobsen, S., Olsbye, U., Tilset, M., Larabi, C., Quadrelli, E.A., Bonino, F., Lillerud, K.P., 2010. Synthesis and stability of tagged UiO-66 Zr-MOFs. Chem. Mater. 22 (24), 6632–6640.

Lee, Dennis T., Zhao, Junjie, Oldham, Christopher J., Peterson, Gregory W., Parsons, a.G.N., 2017. UiO-66-NH_2 Metal−Organic Framework (MOF) nucleation on TiO_2, ZnO, and Al_2O_3 atomic layer deposition-treated polymer fibers: role of metal oxide on MOF growth and catalytic hydrolysis of chemical warfare agent simulantsf. ACS Appl. Mater. Interfaces 9, 44847–44855.

Li, X., Guo, Z., Xiao, C., Goh, T.W., Tesfagaber, D., Huang, W., 2014. Tandem catalysis by palladium nanoclusters encapsulated in metal-organic frameworks. ACS Catal. 4 (10), 3490–3497.

Li, M., Qiu, J., Yang, L., Feng, Y., Yao, J., 2020. Fabrication of TiO2 embedded ZnIn2S4 nanosheets for efficient Cr(VI) reduction. Mater. Res. Bull. 122, 110671.

Liu, E., Du, Y., Bai, X., Fan, J., Hu, X., 2020. Synergistic improvement of Cr(VI) reduction and RhB degradation using RP/g-C_3N_4 photocatalyst under visible light irradiation. Arabian J. Chem. 13 (2), 3836–3848.

Liu, H., Jin, Z., Xu, Z., Zhang, Z., Ao, D., 2015. Fabrication of $ZnIn_2S_4$–g-C_3N_4 sheet-on-sheet nanocomposites for efficient visible-light photocatalytic H_2-evolution and degradation of organic pollutants. RSC Adv. 5 (119), 97951–97961.

Liu, H., Zhang, J., Ao, D., 2018. Construction of heterostructured $ZnIn_2S_4$@NH_2-MIL-125(Ti) nanocomposites for visible-light-driven H_2 production. Appl. Catal. B: Environ. 221, 433–442.

Long, J., Wang, S., Ding, Z., Wang, S., Zhou, Y., Huang, L., Wang, X., 2012. Amine-functionalized zirconium metal–organic framework as efficient visible-light photocatalyst for aerobic organic transformations. Chem. Commun. 48 (95), 11656.

Padhi, D.K., Panigrahi, T.K., Parida, K., Singh, S.K., Mishra, P.M., 2017. Green synthesis of Fe_3O_4/RGO nanocomposite with enhanced photocatalytic performance for Cr(VI) reduction, phenol degradation, and antibacterial activity. ACS Sustain. Chem. Eng. 5 (11), 10551–10562.

Qiu, J., Li, M., Yang, L., Yao, J., 2019. Facile construction of three-dimensional netted ZnIn2S4 by cellulose nanofibrils for efficiently photocatalytic reduction of Cr(VI). Chem. Eng. J. 375, 121990.

Qiu, J., Li, M., Xu, J., Zhang, X.F., Yao, J., 2020. Bismuth sulfide bridged hierarchical Bi_2S_3/BiOCl@$ZnIn_2S_4$ for efficient photocatalytic Cr(VI) reduction. J. Hazard. Mater. 389, 121858.

Shen, L., Liang, S., Wu, W., Liang, R., Wu, L., 2013b. Multifunctional NH_2-mediated zirconium metal-organic framework as an efficient visible-light-driven photocatalyst for selective oxidation of alcohols and reduction of aqueous Cr(VI). Dalton Trans. 42 (37), 13649–13657.

Shen, L., Wu, W., Liang, R., Lin, R., Wu, L., 2013c. Highly dispersed palladium nanoparticles anchored on UiO-66($NH_{(2)}$) metal-organic framework as a reusable and dual functional visible-light-driven photocatalyst. Nanoscale 5 (19), 9374–9382.

Shen, L., Liang, S., Wu, W., Liang, R., Wu, L., 2013a. CdS-decorated UiO–66(NH_2) nanocomposites fabricated by a facile photodeposition process: an efficient and stable visible-light-driven photocatalyst for selective oxidation of alcohols. J. Mater. Chem. A 1 (37), 11473.

Shen, L., Huang, L., Liang, S., Liang, R., Qin, N., Wu, L., 2014. Electrostatically derived self-assembly of NH 2-mediated zirconium MOFs with graphene for photocatalytic reduction of Cr (vi). RSC Adv. 4, 2546–2549.

Shen, L., Luo, M., Liu, Y., Liang, R., Jing, F., Wu, L., 2015. Noble-metal-free MoS_2 co-catalyst decorated UiO-66/CdS hybrids for efficient photocatalytic H_2 production. Appl. Catal. B: Environ. 166–167, 445–453.

Shi, L., Wang, T., Zhang, H., Chang, K., Meng, X., Liu, H., Ye, J., 2015. An Amine-Functionalized Iron(III) metal-organic framework as efficient visible-light photocatalyst for Cr(VI) reduction. Adv. Sci. (Weinh) 2 (3), 1500006.

Su, Y., Zhang, Z., Liu, H., Wang, Y., 2017. $Cd_{0.2}Zn_{0.8}S$@UiO-66-NH_2 nanocomposites as efficient and stable visible-light-driven photocatalyst for H_2 evolution and CO_2 reduction. Appl. Catal. B: Environ. 200, 448–457.

Tong, X., Yang, Z., Feng, J., Li, Y., Zhang, H., 2018. BiOCl/UiO-66 composite with enhanced performance for photo-assisted degradation of dye from water. Appl. Organomet. Chem. 32, (2) e4049.

Vermoortele, F., Bueken, B., Le Bars, G., Van de Voorde, B., Vandichel, M., Houthoofd, K., Vimont, A., Daturi, M., Waroquier, M., Van Speybroeck, V., Kirschhock, C., De Vos, D.E., 2013. Synthesis modulation as a tool to increase the catalytic activity of metal-organic frameworks: the unique case of UiO-66 (Zr). J. Am. Chem. Soc. 135 (31), 11465–11468.

Wang, X.-S., Chen, C.-H., Ichihara, F., Oshikiri, M., Liang, J., Li, L., Li, Y., Song, H., Wang, S., Zhang, T., Huang, Y.-B., Cao, R., Ye, J., 2019. Integration of adsorption and photosensitivity capabilities into a cationic multivariate metal-organic framework for enhanced visible-light photoreduction reaction. Appl. Catal. B: Environ. 253, 323–330.

Wang, X., Liu, J., Leong, S., Lin, X., Wei, J., Kong, B., Xu, Y., Low, Z.X., Yao, J., Wang, H., 2016. Rapid construction of ZnO@ZIF-8 heterostructures with size-selective photocatalysis properties. ACS Appl. Mater. Interfaces 8 (14), 9080–9087.

Wu, P., Jiang, M., Li, Y., Liu, Y., Wang, J., 2017. Highly efficient photocatalytic hydrogen production from pure water via a photoactive metal–organic framework and its PDMS@MOF. J. Mater. Chem. A 5 (17), 7833–7838.

Xiao, J.D., Shang, Q., Xiong, Y., Zhang, Q., Luo, Y., Yu, S.H., Jiang, H.L., 2016. Boosting photocatalytic hydrogen production of a metal–organic framework decorated with platinum nanoparticles: The platinum location matters. Angew. Chem. Int. Ed. 55 (32), 9389–9393.

Xie, B., Shan, C., Xu, Z., Li, X., Zhang, X., Chen, J., Pan, B., 2017. One-step removal of Cr(VI) at alkaline pH by UV/sulfite process: Reduction to Cr(III) and in situ Cr(III) precipitation. Chem. Eng. J. 308, 791–797.

Xing, Y., Chen, X., Wang, D., 2007. Electrically regenerated ion exchange for removal and recovery of Cr (VI) from wastewater. Environ. Sci. Technol. 41, 1439–1443.

Xu, S., Dai, J., Yang, J., You, J., Hao, J., 2018. Facile synthesis of novel CaIn(2)S(4)/ZnIn(2)S(4) composites with efficient performance for photocatalytic reduction of Cr(VI) under simulated sunlight irradiation. Nanomaterials (Basel) 8 (7).

Xu, Y., Lv, M., Yang, H., Chen, Q., Liu, X., Fengyu Wei, F.W., 2015. $BiVO_4$/MIL-101 composite having the synergistically enhanced visible light photocatalytic activity. RSC Adv. 5 (54), 43473–43479.

Yang, J., Zhang, F., Wang, X., He, D., Wu, G., Yang, Q., Hong, X., Wu, Y., Li, Y., 2016. Porous molybdenum phosphide nano-octahedrons derived from confined phosphorization in UIO-66 for efficient hydrogen evolution. Angew. Chem. Int. Ed. Engl. 55 (41), 12854–12858.

Zhang, G., Chen, D., Li, N., Xu, Q., Li, H., He, J., Lu, J., 2018. Preparation of $ZnIn_2S_4$ nanosheet-coated CdS nanorod heterostructures for efficient photocatalytic reduction of Cr(VI). Appl. Catal. B: Environ. 232, 164–174.

Zhang, Y.C., Li, J., Zhang, M., Dionysiou, D.D., 2011b. Size-tunable hydrothermal synthesis of SnS_2 nanocrystals with high performance in visible light-driven photocatalytic reduction of aqueous Cr(VI). Environ. Sci. Technol. 45 (21), 9324–9331.

Zhang, Y.C., Du, Z.N., Li, K.W., Zhang, M., Dionysiou, D.D., 2011a. High-performance visible-light-driven $SnS_{(2)}$/$SnO_{(2)}$ nanocomposite photocatalyst prepared via in situ hydrothermal oxidation of $SnS_{(2)}$ nanoparticles. ACS Appl. Mater. Interfaces 3 (5), 1528–1537.

Zhang, Y.C., Yao, L., Zhang, G., Dionysiou, D.D., Li, J., Du, X., 2014. One-step hydrothermal synthesis of high-performance visible-light-driven SnS_2/SnO_2 nanoheterojunction photocatalyst for the reduction of aqueous Cr(VI). Appl. Catal. B: Environ 144, 730–738.

Zhao, C., Dai, X., Yao, T., Chen, W., Wang, X., Wang, J., Yang, J., Wei, S., Wu, Y., Li, Y., 2017. Ionic exchange of metal-organic frameworks to access single nickel sites for efficient electroreduction of CO_2. J. Am. Chem. Soc. 139 (24), 8078–8081.